A sol-gel pretreatment combined strategy for constructing cobalt-embedded and nitrogen-doped carbon matrix with high-density active sites as bifunctional oxygen reduction and evolution electrocatalysts

Depeng Wang, Xintao Zuo, Huiling Liu[*], Cheng Wang

Institute for New Energy Materials and Low-Carbon Technologies, School of Materials Science and Engineering, Tianjin Key Laboratory of Advanced Functional Porous Materials, Tianjin University of Technology, Tianjin 300384, China

ARTICLE INFO

ABSTRACT

Developing highly efficient bifunctional oxygen electrocatalysts via cost-effective methods is of great significance for energy storage and conversion systems but still full of challenges. In this work, a simple and eco-friendly method which involves a sol-gel pretreatment on multiple precursors and subsequent pyrolysis is designed to synthesize Co nanoparticles embedded and nitrogen-doped porous carbon (Co@NC). The sol-gel pretreatment ensures the high dispersion of all precursors, which is beneficial to the formation of uniform and highly dense active sites. After pyrolysis, acid treatment removes the unencapsulated Co nanoparticles on the surface to form porous structure and increase the mass activity. Benefiting from the synthetic strategy, the porous Co@NC-850 with large surface area, high density of active sites (graphitic N, pyridinic N and Co-N$_x$) exhibits comparable oxygen reduction performance ($E_{1/2}$ = 0.85 V vs. reversible hydrogen electrode) to that of commercial Pt/C and better oxygen evolution activity (with an overpotential of 350 mV at 10 mA cm^{-2}) with respect to RuO$_2$. The potential gap ΔE (between the oxygen evolution potential at 10 mA cm^{-2} and oxygen reduction $E_{1/2}$) for Co@NC-850 is only 0.73 V. Compared with the state-of-the-art bifunctional oxygen electrocatalysts, Co@NC-850 shows obvious advantages in bifunctional activity and durability. The results in the present work will shed light on the development of other carbonaceous materials as the bifunctional oxygen electrocatalysts for energy storage and electrochemical devices.

© 2021 Elsevier B.V. All rights reserved.

1. Introduction

The excessive consumptions of fossil fuels have caused global energy crisis and related environmental issues [1,2]. Thus the development of renewable, clean and economic energy systems becomes more significance to replace the traditional energy sources. Due to the high energy density and environmental friendliness, fuel cells [3], water splitting electrolyzers [4,5] and metal-air batteries [6,7] have recently attracted extensive attention in novel energy devices. Oxygen reduction reaction (ORR) and oxygen evolution reaction (OER) are the most important reactions in these devices. However, the intrinsic multiple electron-transfer reaction steps [8—10] typically resulted in sluggish reaction kinetics and limit the large-scale applications. Pt- [11,12] and IrO$_2$/RuO$_2$-based [13,14] noble metal/metal oxide electrocatalysts have been widely used as

the active electrodes for ORR and OER, respectively. However, the high cost, scarcity, and poor durability hindered the large-scale application of the noble-metal based electrocatalysts. Simultaneously, Pt-based catalysts only show high efficiency for ORR. And IrO$_2$/RuO$_2$ based catalysts are only applicable for OER. Hence, economic, effective and stable bifunctional ORR/OER electrocatalysts without precious metal are urgently needed for paving the applications of oxygen reaction related energy systems.

Carbon-based materials have attracted extensive interest as electrocatalysts due to their high conductivity, chemical stability and cost-effectiveness [15—18]. Nevertheless, the pristine carbon structures typically show unsatisfied activity towards ORR and OER because of the electroneutral carbon atoms [19]. Hence, doping heteroatoms (e.g., N, P, and S) with different electronegativities into the carbon matrix has been widely designed to adjust the electronic structure [20—23]. Specifically, the strong electron affinity of N inhibits the electron density of adjacent C-atoms, leading to positive charge distribution on C-atoms (C$^+$), thereby modifying the adsorptions of O-involved reactants/intermediates and improving the ORR

and OER activities [24,25]. Further incorporation of transition metals (Fe, Co, Ni, etc.) for constructing transition metals and nitrogen co-doped carbonaceous catalysts (M-N-C) has then been demonstrated to exhibit more significant enhancement in the performance of the oxygen electrocatalysis [26,27]. Among them, Co-N-C based electrocatalysts have been extensively studied since Raymond firstly reported the ability of cobalt phthalocyanine with a Co-N$_4$ center to catalyze ORR in 1964 [28]. Although various Co-N-C materials have been constructed to improve the oxygen electrocatalysis performance, the coupling between Co and N-doped carbon, and Co-N (or Co-N-C) sites are consistently believed to play a crucial role in enhancing the ORR/OER activity. For example, for typical Co embedded and N-doped Co-N-C materials, the electronic interactions between the N-C shell and encapsulated Co-N/O moieties could optimize oxygen adsorption behaviors and therefore enhance the ORR and OER kinetics [29–31]. Besides, the coordination types of Co-N sites are reported to have a great influence on the oxygen electrocatalysis. Pyridinic-N-Co bond is demonstrated to be able to optimize the adsorption of oxygen-containing intermediates (O*, OH*, OO*, OOH*) to promote the reversible ORR/OER process [32]. Another example is that the precise Co-N$_2$ coordination in a Co-C$_3$N$_4$/CNT electrocatalyst is confirmed to be the intrinsic active center based on experimental and DFT results [33]. However, tremendous efforts are already being made, and more will need to further develop highly efficient Co-N-C electrocatalysts for practical applications in the future.

The synthetic strategies for M-N-C materials generally involve the pyrolysis from multiple precursors [34], metal-organic frameworks derived route [35–38], hard/soft-template method [39,40] and direct compositing transition metals with carbon nanotubes/graphene [41,42]. Among them, using multiple precursors as the sources of metal, N and carbon support is a simple, inexpensive, and versatile approach. Nowadays, many studies continue to optimize the compositions of the precursors and pyrolysis conditions for constructing highly effective M-N-C materials as oxygen electrocatalysts [43,44]. Herein, we combine a sol-gel method for multiple precursors pretreating with following pyrolysis to synthesize a Co-embedded and N-doped porous carbonaceous material as the bifunctional electrocatalyst for ORR and OER. The composition of the precursors including cobalt acetate, citric acid and urea for preparing ORR-OER bifunctional electrocatalyst has not been reported before. The citric acid with abundant carbon atoms and powerful combining capacity to form complexes is selected as the carbon source. The urea is used for in-situ introducing N source through the reaction with citric acid. Besides, the introduced N could chelate with Co ions and thus facilitate the uniform dispersion of Co species. Therefore, the involved sol-gel pretreatment benefits the high dispersion of all precursors, which garners the advance in constructing catalysts with highly uniform and dense active Co-N-C sites. After pyrolysis, an acid-washing step is employed to remove unencapsulated Co nanoparticles to form porous structure and increase the mass activity. Benefiting from the synthetic strategy, the porous Co@NC-850 with large surface area, high density of active sites (graphitic N, pyridinic N and Co-N$_x$) exhibits comparable ORR activity ($E_{1/2}$ = 0.85 V vs. reversible hydrogen electrode

(RHE)) to that of commercial Pt/C and better OER activity (with an overpotential of 350 mV at 10 mA cm^{-2}) with respect to RuO$_2$. In addition, the Co@NC-850 delivers a small metric ΔE of only 0.73 V in the evaluation of the ORR-OER bifunctionality, which is also comparable to that of the recently developed state-of-the-art bifunctional oxygen electrocatalysts. This work provides a facile and effective way to construct transition metals modified and heteroatom co-doped catalysts, shedding lights on designing high-efficient electrocatalysts for energy storage and related devices.

2. Experimental section

2.1. Chemicals

Cobalt acetate tetrahydrate (Co(CH$_3$COO)$_2$.4H$_2$O, 99.5%), citric acid (HOOCCH$_2$C(OH)(COOH)CH$_2$COOH), urea (CO(NH$_2$)$_2$), ethanol (C$_2$H$_5$OH) and hydrochloric acid (HCl) were obtained from Shanghai Chemical Reagents, China. Nafion was acquired from Sigma-Aldrich. The commercial Pt/C catalyst is 20% by wt. of ~3 nm Pt nanoparticles loading on Vulcan XC-72 carbon support. RuO$_2$ was supplied from Aladdin Chemical Reagent Company (Shanghai, China). All of the chemicals involved in the experiments were analytical grade and used without further purification. Deionized water (18 MΩ·cm) was used throughout all the experiments.

2.2. Synthesis of Co@NC-T

The Co@NC-T (T = 650, 750, 850 and 950, notes the pyrolysis temperature) materials were prepared through a simple sol-gel pretreatment followed by pyrolysis approach. Firstly, citric acid (5 mmol), urea (167 mmol) and cobalt acetate tetrahydrate (3 mmol) were dissolved in a mixed solvent of distilled water and ethanol (200 mL, v/v (H$_2$O/ethanol) = 1:3). Secondly, the mixture was placed in a water bath under continuous agitation at 80 °C until the formation of a gel. Then the gel was dried at 110 °C for 8 h. Subsequently, the resultant precursors were calcined at 350 °C for 4 h and then 650/750/850/950 °C for 5 h under Ar atmosphere with a heating rate of 5 °C min^{-1}. Thirdly, the obtained black powders were treated with HCl solution (6 M) for 24 h at 60 °C to remove the redundant Co nanoparticles. Finally, the Co@NC-T materials were obtained after washing with distilled water and drying at 60 °C for 10 h. In addition, reference samples synthesized by simply mixing the raw materials in ethanol without the sol-gel pretreatment, and then calcining the precursor under the same pyrolysis step were also prepared and referred to as CoNC-850.

3. Results and discussion

3.1. Synthesis and structure of Co@NC-T

The fabrication process of cobalt embedded and nitrogen-doped carbon nanosheets (Co@NC-T, T = 650, 750, 850 and 950, notes the pyrolysis temperature) is illustrated in Fig. 1. Typically, a sol-gel
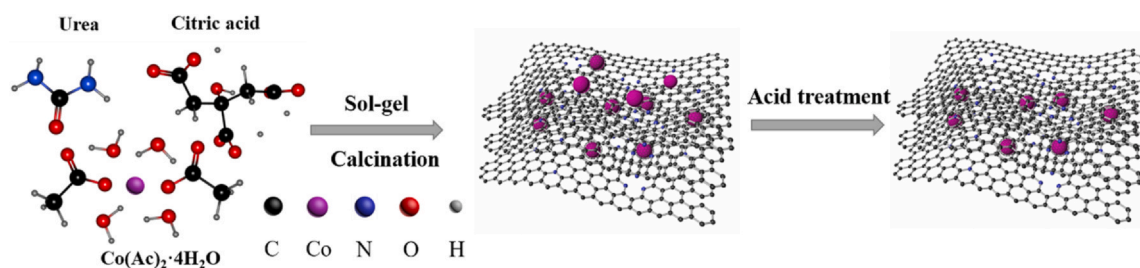
Fig. 1. The schematic illustration for the preparation of the Co@NC-T.

precursor was first prepared by mixing citric acid, urea and cobalt acetate in water and ethanol and keeping the mixture stirred at 80 °C. In this sol-gel pretreatment step, urea is firstly hydrolyzed into NH_3 and CO_2 upon the heating. Then, the NH_3 reacts with —COOH of citric acid to form —$COONH_4$ which spontaneously transforms to —$CONH_2$, in-situ introducing N into the carbon source (citric acid). The formed —NH_2 could chelate with Co^{2+} ions, facilitating the uniform distribution of Co species in the precursor. As a result, based on the citric acid molecules, C, N and Co elements are highly dispersed after the sol-gel pretreatment [45–47]. With abundant functional groups containing polar (O and N) and H atoms, hydrogen bonds like N—H—O, N—H—N and O—H—O probably form and the reactant molecules could cross into a 3D network structure which becomes gel-like state (as shown by the photos in Fig. S1). The hydrogen bonds are responsibility for providing the certain mechanical strength to the sol-gel precursor. After dried at 110 °C for 8 h, the obtained pink powder was pyrolyzed at 350 °C for 4 h and T °C for 5 h under Ar atmosphere. During the pyrolysis process, the organic molecules further combine through the dehydration-condensation reactions between —H and —OH/—NH_2 groups and then thermally decompose and carbonize to carbon matrix. The pre-formed 3D network can act as the template for the carbonized framework and confine the Co nanoparticles in the Co@NC-T. The coordination between Co and N ensures the in-situ formation of high-density Co-N_x sites in the pyrolysis step. Subsequently, the black powder was treated with HCl to dissolve the surface unencapsulated Co particles, remaining Co nanoparticles embedded in nitrogen-doped porous carbon nanosheets. Reference samples (denoted as CoNC-850) were also prepared through the similar synthetic procedure without the sol-gel pretreatment step.

The morphology and structure of Co@NC-T were observed by scanning electron microscopy (SEM) and transmission electron microscopy (TEM). As shown in Figs. 2a, b and S2a–c, the SEM images of Co@NC-T present similar 2D sheet structures with numerous crumples and pores, which are beneficial for exposing more active sites [48]. The TEM images in Figs. 2c, d and S2d–f clearly exhibit the difference in the structures of the Co@NC-T. The TEM images of Co@NC-650, 750 and 850 (Figs. 2d and S2d, e) show that as the pyrolysis temperature increases, the size of the cobalt nanoparticles also increases gradually from about 32–38 nm (Fig. S3a–c). Especially when the temperature was set up to 950 °C, the size of cobalt nanoparticles obviously increased to ~57.8 nm (Figs. S2f and S3d). This is mainly due to the fact that Co atoms are more likely to migrate to the surface at high temperatures and aggregate into large cobalt particles, then rendering the metallic particles easier to be exposed and removed by acid washing [49,50]. Thus, for the distribution density of the metal nanoparticles, higher pyrolysis temperature leads to lower density, which is consistent with the Co contents from the results of inductively coupled plasma mass spectrometry (ICP-MS, Table S1). When the calcination temperature increases from 650° to 950 °C, the cobalt content decreases from 23.01 to 3.15 wt%. To further determine the structural information of the Co@NC-T, high-resolution TEM (HRTEM) characterization of Co@NC-850 as a typical sample was further performed. As shown in Fig. 2e, crystalline nanoparticles with dark contract are embedded in the low-contrast background. The inner lattice fringes with a d-spacing of 0.203 nm belong to the (111) plane of face-centered cubic (fcc) phase Co, and the surrounding wavy lattice fringes with a d-spacing of 0.34 nm correspond to the (002) plane of graphitic carbon [51,52]. The HRTEM results clearly confirm that the Co nanoparticles are tightly encapsulated by carbon layers due to the catalytic action of Co towards carbon graphitization. The carbon layers are expected to protect the Co nanoparticles from etching during oxygen electrocatalysis, contributing to the stability of catalysts in ORR and OER [51,53,54]. Furthermore, Fig. 2f shows the high-angle annular dark-field scanning transmission electron microscopy (HAADF-STEM)

image and the energy dispersive X-ray spectroscopy (EDS) mapping image of the Co@NC-850. The presence of bright particles in Fig. 2f indicates that tiny Co nanoparticles are evenly distributed on the graphitized porous carbon. At the same time, N element is observed to disperse homogeneously throughout the Co@NC-850.

XRD measurement was conducted to explore the crystal structures of Co@NC-T. In Fig. 3a, the diffraction peaks at $2\theta \approx 44.2°$, $51.6°$, and $75.8°$ are assigned to the (111), (200) and (220) planes of fcc Co in the Co@NC-T, respectively, which is in good agreement with JCPDS card 15-0806. There is a broad diffraction peak at $2\theta \approx 26.1°$, corresponding to the (002) plane of graphite carbon. It is clearly observed that the peak intensity of graphite carbon (002) becomes stronger and narrower as the pyrolysis temperature increasing from 650 °C to 950 °C. This indicates that higher pyrolysis temperature leads to more ordered graphite structure, which contributes to improving the conductivity of the catalysts. The graphitization degree of the carbon matrixes was further verified by Raman spectra (Fig. 3b). The D-band at 1354 cm^{-1} is ascribed to the introduced defects in the graphene framework, and the G-band at 1591 cm^{-1} represents the sp^2 graphite carbon. The ratios of their band intensities (I_D/I_G) decrease from 1.05 to 0.60 as the pyrolysis temperature increasing from 650 °C to 950 °C, which reveals a higher graphitization degree at higher pyrolysis temperature. This is consistent with the XRD patterns. In general, a high graphitization degree is beneficial to increase the conductivity and enhance electron transfer of an electrocatalyst, while defect sites can tune the electronic and surface properties of carbonaceous materials and optimize the free energies of different electrochemical catalysis steps [52,54]. However, the graphitization degree generally trades off the number of defect sites. A balance between these two factors is highly desirable for optimizing the catalytic activity. The specific surface areas and pore structures of the catalysts were characterized by N_2 adsorption/desorption measurements. Fig. 3c shows the type IV isotherm curves and distinct type-H4 hysteresis loops ($P/P_0 > 0.45$), indicating the existence of mesopores generated by crumple structure. The pore-size distribution plot (Fig. 3d) confirms that the pore sizes are located at 3–6, 10–12, 12–14 and 16–18 nm, showing a hierarchical mesoporous structure [55]. Notably, according to Brunauer-Emmett-Teller (BET) calculation, Co@NC-850 exhibits the highest specific surface area (363.7 m^2/g) and pore volume (0.608 cm^3/g) as shown in Table S2. The hierarchical mesoporous structure along with a large specific surface area is in favor of exposing active sites and facilitating the mass transport during the catalytic process. The thermal stability of the synthesized catalysts is important for practical applications. Thermogravimetric analysis (TGA) of the Co@NC-850 was measured in Ar from room temperature to 900 °C with a heating rate of 5 °C min^{-1}. As depicted in Fig. S4, the residual Mass% of Co@NC-850 is ~93.36 when the temperature reaches around 900 °C, demonstrating the robust stability under high temperature.

The surface compositions and chemical states of the Co@NC-T were explored through X-ray photoelectron spectroscopy (XPS) measurement. The survey XPS spectra (Fig. 4a) confirm the coexistence of C, N, Co, and O elements in the Co@NC-T. The appearance of O signals is probably due to the physical adsorption of oxygen species and partial oxidation of the surface materials exposed to the air [24,25,56]. The high-resolution C 1s spectra in Fig. 4b can be devided into four peaks located at about 284.7, 285.2, 286.7 and 289.1 eV, corresponding to C—C, C—N, C=O and O=C—O species (Table S3), respectively [9,44,53,57]. The presence of C—N part indicates that N is successfully doped into the carbon skeleton. As for the high-resolution Co 2p XPS spectra, Fig. 4c and Table S3 reveals the presence of Co^0 (~779.1 eV), Co^{2+} (Co $2p_{3/2}$ ~781.4 eV, Co $2p_{1/2}$ ~796.8 eV), Co^{3+} (Co $2p_{3/2}$ ~780.2 eV, Co $2p_{1/2}$ ~795.0 eV) and shakeup satellite [9,43,58–61]. The presence of Co^{2+} and Co^{3+} is mostly attributed to the formation of Co-N_x species, since Co interacts strongly with N at high temperatures [24,25,56]. The Co-N bond has
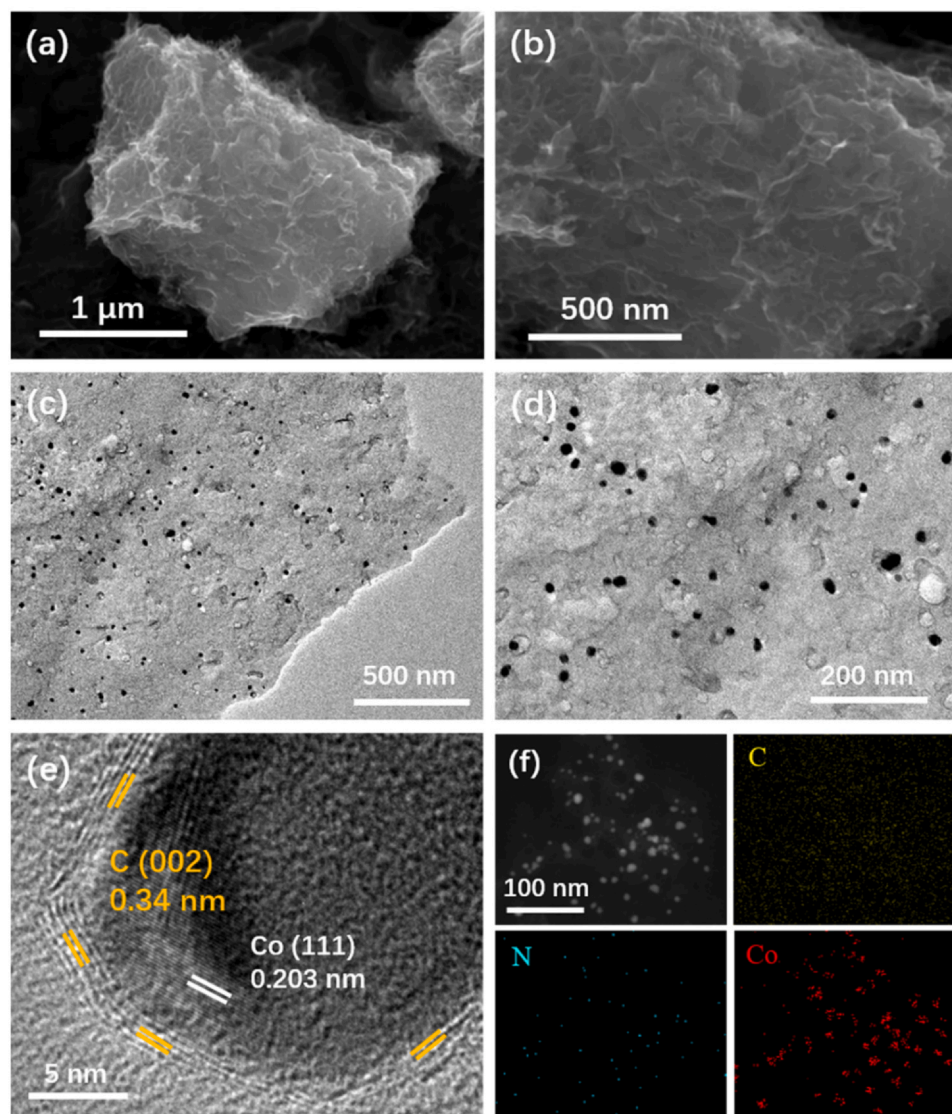
Fig. 2. (a and b) SEM, (c and d) TEM and (e) HRTEM images of the as-prepared Co@NC-850. (f) HAADF-STEM image and the corresponding elemental mapping of Co@NC-850.

been reported to be a highly effective active site for catalyzing the OER and ORR [43,52,58]. Partial surface oxidation of Co nanoparticles probably also makes a contribution to the Co^{2+} and Co^{3+} signals, because Co can be easily oxidized in the air [24,25]. As displayed in Fig. 4d, the N 1s of Co@NC-*T* samples can be classified into five types of N (Table S3), including pyridinic N (~398.5 eV), Co-N_x (~399.2 eV), pyrrolic N (~400.2 eV), graphitic N (~401.3 eV) and oxidized N (~404.4 eV), respectively [25,44,62,63]. Up to now, the authentic role of different types of N is still a controversial debate, which is ponderable but difficult to achieve. One of the conclusive consequences to be accepted is that Co-N_x, pyridinic N and graphite N play key roles in promoting ORR and OER [44,58,64]. As shown in Fig. S5a and Table S4, the relative content of potential nitrogen active species (Co-N_x, pyridinic N and graphitic N) for Co@NC-850 is about 92.80%, which is much higher than those of Co@NC-650 (66.20%), Co@NC-750 (84.22%) and Co@NC-950 (86.66%). Moreover, according to the elemental analysis (Table S1), Co@NC-850 possesses the highest absolute content of Co-N_x (0.93 wt%) among the Co@NC-*T* (Fig. S5b and Table S4). Obviously, it is found that Co-N_x, pyridinic N and graphite N occupy the dominant proportion in Co@NC-850, which is expected to make the main contribution to the excellent performance.

All the above results reveal the advantages of the sol-gel pretreatment in forming Co and N co-incorporated carbon matrix with 2D sheet-like structure, uniform distribution of Co nanoparticles, large specific surface area and high-density active sites. To further confirm the advantages, the structural change of CoNC-850 which was prepared without of the sol-gel pretreatment step is also identified. Fig. S6a, b shows the SEM and TEM images of the CoNC-850. Compared with the Co@NC-850, the carbon matrix in CoNC-850 displays irregular shapes and agglomeration. Besides, the distribution of Co nanoparticles in CoNC-850 is less uniform than that in Co@NC-850. According to the histogram in Figs. S6c and S3c, the size of Co nanoparticles in Co@NC-850 varies from 33 to 38 nm (with an average value of 35.9 nm), while the size distribution of Co nanoparticles in the CoNC-850 (from 10 to 150 nm with an average value of 48.1 nm) is much wider. N_2 adsorption/desorption measurement on the CoNC-850 was also conducted. As shown in Fig. S6d, the CoNC-850 also exhibits the type IV isotherm curve and distinct type-H4 hysteresis loop. However, the specific surface area of the CoNC-850 according to BET calculation (194.2 m^2/g, Table S2) is much lower than that of Co@NC-850 (363.7 m^2/g). As for the XPS, the CoNC-850 displays similar Co and N species with those of the Co@NC-850 as shown in Fig. S6e, f and Table S3. But the CoNC-850
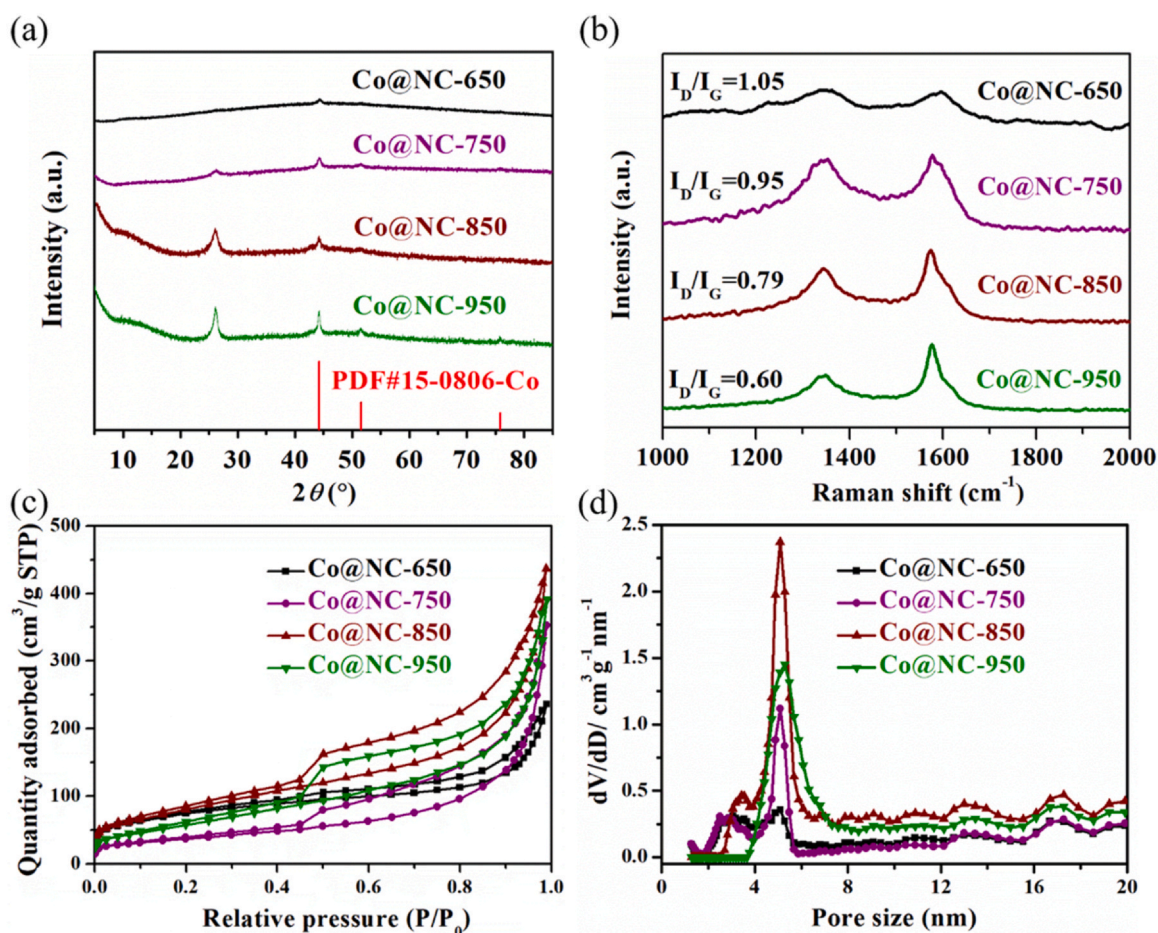
Fig. 3. (a) XRD patterns, (b) Raman spectra, (c) N_2 adsorption-desorption isotherm curves, and (d) pore size distribution of Co@NC-T (T = 650, 750, 850 and 950).

presents a lower ratio of the electrocatalytically active N species (Table S4), i.e. the sum of Pyri-N, Grap-N and Co-N_x (72.32%), than that of Co@NC-850 (92.80%). Therefore, the sol-gel pretreatment step plays a crucial role in constructing the Co@NC-850 with desirable structural features.

3.2. ORR performance of Co@NC-T

The electrocatalytic performance of the Co@NC-T (T = 650, 750, 850 and 950) towards ORR was first investigated through cyclic voltammetry (CV) measurement conducted in O_2/N_2 saturated 0.1 M KOH electrolyte. An Ag/AgCl electrode was used as the reference electrode, and all the measured potentials are converted to RHE based on calibration shown in the Supporting Information [65,66]. The CV curves (Fig. 5a) show that each Co@NC-T exhibits a pronounced reduction peak in O_2-saturated KOH but no redox feature was observed in N_2-saturated electrolyte, implying the intrinsic ORR activity of the Co@NC-T. Specifically, the Co@NC-850 shows a reduction peak located at about 0.80 V (vs. RHE, the following potentials are all referred to RHE without specific notes), which is more positive than 0.76, 0.79 and 0.77 V of Co@NC-650, 750 and 950, respectively. Note that the 0.80 V of Co@NC-850 is comparable to 0.80 V of commercial benchmark Pt/C. The result implies the superior ORR activity of the Co@NC-850. As shown in Fig. 5b, the superior ORR activity of the Co@NC-850 is further confirmed by the linear sweep voltammetry (LSV) polarization curves. The Co@NC-850 exhibits the most positive onset and half-wave potentials (0.95 V, $E_{1/2}$ = 0.85 V) with respect to the CoNC-850 (0.87 V, $E_{1/2}$ = 0.75 V), Co@NC-650 (0.91 V, $E_{1/2}$ = 0.82 V), Co@NC-750 (0.94 V,

$E_{1/2}$ = 0.83 V), Co@NC-950 (0.94 V, $E_{1/2}$ = 0.82 V) and even Pt/C (0.94 V, $E_{1/2}$ = 0.83 V), which is also better than most reported Co-based carbonaceous ORR electrocatalysts (Table S5). Additionally, the diffusion-limited current density (J_d, at 0.2 V) of Co@NC-850 is determined to be 5.31 mA cm^{-2}, which is higher than the 4.53 mA cm^{-2} for Co@NC-650, 4.65 mA cm^{-2} for Co@NC-750 and 4.70 mA cm^{-2} for Co@NC-950. The result suggests that Co@NC-850 delivers an improved mass transport during the ORR process [9]. Tafel slopes (Fig. S7) of the plots derived from polarization curves were calculated to analyze the ORR kinetics. Co@NC-850 exhibits the smallest Tafel slope of 57 mV dec^{-1}, indicating a preferable ORR kinetics with the first electron transfer reaction as the rate-determining step [67]. The turnover frequencies (TOF) were calculated to compare the intrinsic activity of Co@NC-T electrodes for ORR [66,68]. As shown in Fig. S8, the Co@NC-850 exhibits a high TOF of 0.011 s^{-1} (0.8 V vs. RHE) for ORR, which is higher than that of Co@NC-650 (0.002 s^{-1}), Co@NC-950 (0.004 s^{-1}) and Co@NC-950 (0.010 s^{-1}), suggesting a faster ORR kinetics.

The electron transfer number per oxygen molecule (n) and kinetic limiting current density (J_K) of the ORR process for the Co@NC-T were studied. The polarization curves (Fig. 5c) were recorded at 400—2500 rpm according to Koutechy-Levich (K-L) equation. The K-L plots (the inset in Fig. 5c) exhibit good linearity between the current density and the rotation speed, indicating a first-order reaction kinetics relative to the concentration of dissolved oxygen. Meanwhile, the consistent slopes indicate the similar electron transfer mechanisms for ORR at the various redox potentials [24,69]. In the potential range of 0.3—0.6 V, the electron transfer number of Co@NC-850 is determined to be $n \approx 3.96$ and much higher than those of Co@NC-650 (3.64, Fig. S9a, b), Co@NC-750 (3.52, Fig. S9c, d) and Co@NC-
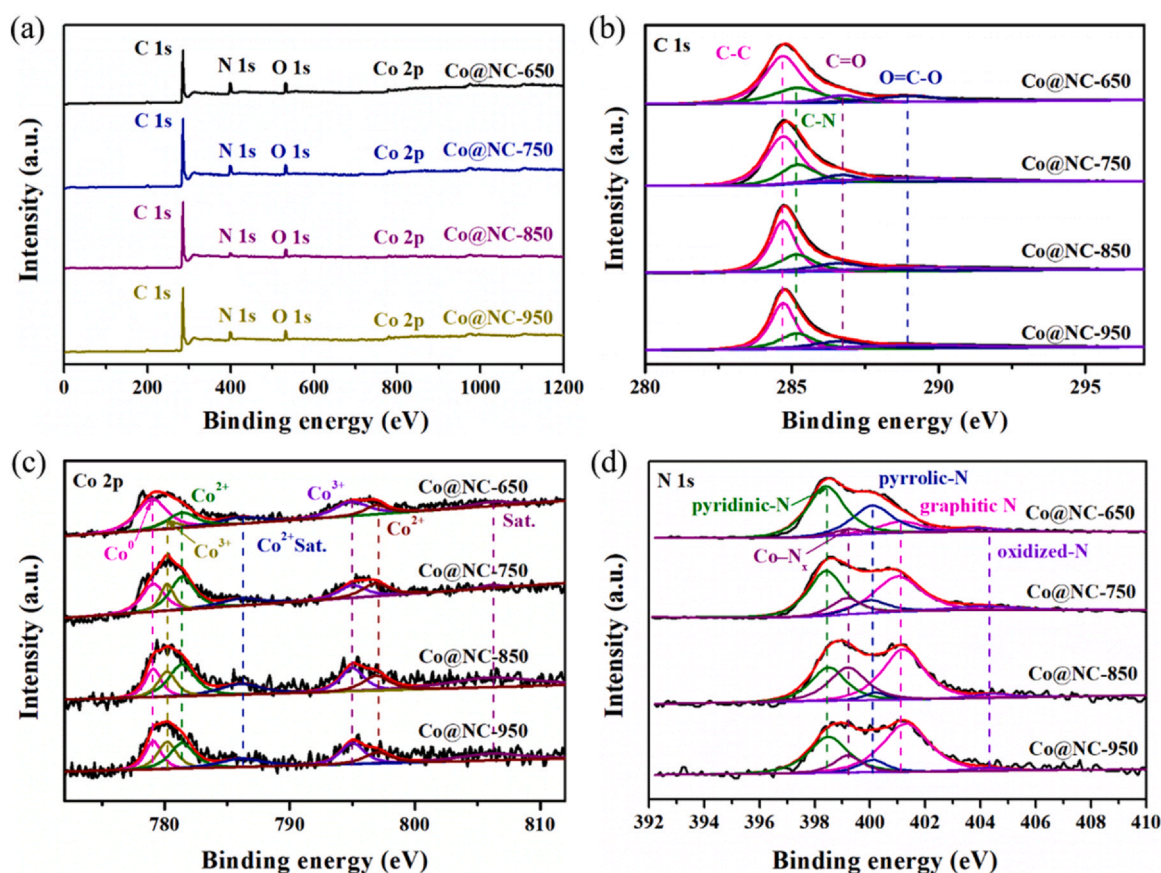
Fig. 4. (a) XPS survey spectra and high resolution XPS of (b) C 1s (c) Co 2p and (d) N 1s of Co@NC-*T* (*T* = 650, 750, 850 and 950).

950 (3.43, Fig. S9e, f). The results confirm that the surface of Co@NC-850 goes through a four-electron transfer ORR process with OH^- as the final product in alkaline electrolyte. In contrast, other Co@NC counterparts proceed with mixed two- and four-electron reactions pathway. This conclusion is further confirmed by the results of the rotating ring-disk electrode (RRDE) test. Based on RRDE data (Fig. 5d), the electron transfer number of Co@NC-850 is calculated to be 3.99 with an extremely low H_2O_2 yield of around 0.65%. The Co@NC-650, 750 and 950 again give lower electron transfer numbers and higher H_2O_2 yields as summarized in Figs. S10 and S11a. With a desirable four-electron transfer pathway, the Co@NC-850 shows a high J_K (at 0.80 V, based on geometric area) of 39.28 mA cm^{-2}, corresponding to 1.5, 1.55 and 3.22 times higher than the values of Co@NC-650, 750 and 950, respectively, and even 3.17-fold of the commercial Pt/C (Fig. S11b). The comparison of the half-wave potential ($E_{1/2}$) and J_K among Co@NC-*T* and Pt/C in Fig. S11b confirms the superior ORR performance of Co@NC-850.

The superior electrocatalytic activity of Co@NC-850 should be ascribed to its special chemical composition and structural feature. For metal/nitrogen co-incorporated carbonaceous (M-N-C) electrocatalysts, although the discussion on the role of N-related species has not been unanimous, graphitic N, pyridinic N and M-N$_x$ sites have been intensively considered as the active centers for ORR [44,58,64]. In our case, the highest sum of the relative contents of graphitic N, pyridinic N and Co-N$_x$ for the Co@NC-850 (Fig. S5b and Table S4) is primarily believed to be reasonable to the observed improved ORR activity. In addition, M-N$_x$ has been reported to be a crucial active site for facilitating both the adsorption of O_2 molecule and the subsequent breaking of O=O bond [62,70]. According to the elemental analysis and N 1s XPS spectra (Tables S1, 4), the Co@NC-850 also possesses the highest Co-N$_x$ content of 0.93 wt% with respect to 0.42, 0.69 and 0.11 wt% for Co@NC-650, 750 and 950,

respectively. With a high content of active sites, the largest surface area (as shown in Table S2) of Co@NC-850 further ensures the exposure of reactive centers, which is verified by the comparison on the electrochemically active surface area (ECSA) of the Co@NC-*T*. The ECSA is typically represented by the electrochemical double-layer capacitance (C_{dl}) by testing CV curves at different scan rates (Fig. S12). As shown in Fig. S13, the C_{dl} of Co@NC-850 is 10 mF cm^{-2}, higher than those of Co@NC-650 (8.5 mF cm^{-2}), Co@NC-750 (9.3 mF cm^{-2}) and Co@NC-950 (8.45 mF cm^{-2}), suggesting the efficient exposure of active sites on the Co@NC-850 catalyst for ORR. The Nyquist plots and equivalent circuit models of the samples for ORR are shown in Fig. S14a. The charge-transfer resistances (R_{ct}) and solution resistances (R_s) of the samples for ORR and OER are calculated according to the models and compared in Table S6. The Co@NC-850 shows the lowest R_{ct} value for the ORR (33.26 Ω), revealing the fast electron transfer and kinetic behavior on Co@NC-850. The corresponding Bode plots of the electrodes are displayed in Fig. S14b, c. The low peak phase angle (Fig. S14b) and drastic drop in the impedance magnitude (Fig. S14c) of the Co@NC-850 further confirm the favorable ORR on the surface of Co@NC-850.

The durability of Co@NC-850 and Pt/C catalysts was evaluated by current-time (*i*–*t*) chronoamperometric method at 0.6 V in O_2-saturated 0.1 M KOH solution. As depicted in Fig. 5e, the Co@NC-850 maintains 94.6% of its initial current after a continuous operation with 25 h, while the commercial Pt/C can only retain 67.2% of its initial current value, indicating the considerable stability of the Co@NC-850. This is most likely attributed to the protection effect of the graphitic carbon layer surrounding the Co nanoparticles on inhibiting the corrosion of active sites. Meanwhile, the stability of Co@NC-850 is further indicated by the LSV curves before and after CV scan for 5000 cycles at 1600 rpm. A negligible catalytic degradation (6 mV) can be observed for Co@NC-850 (Fig. S15a). In contrast, an
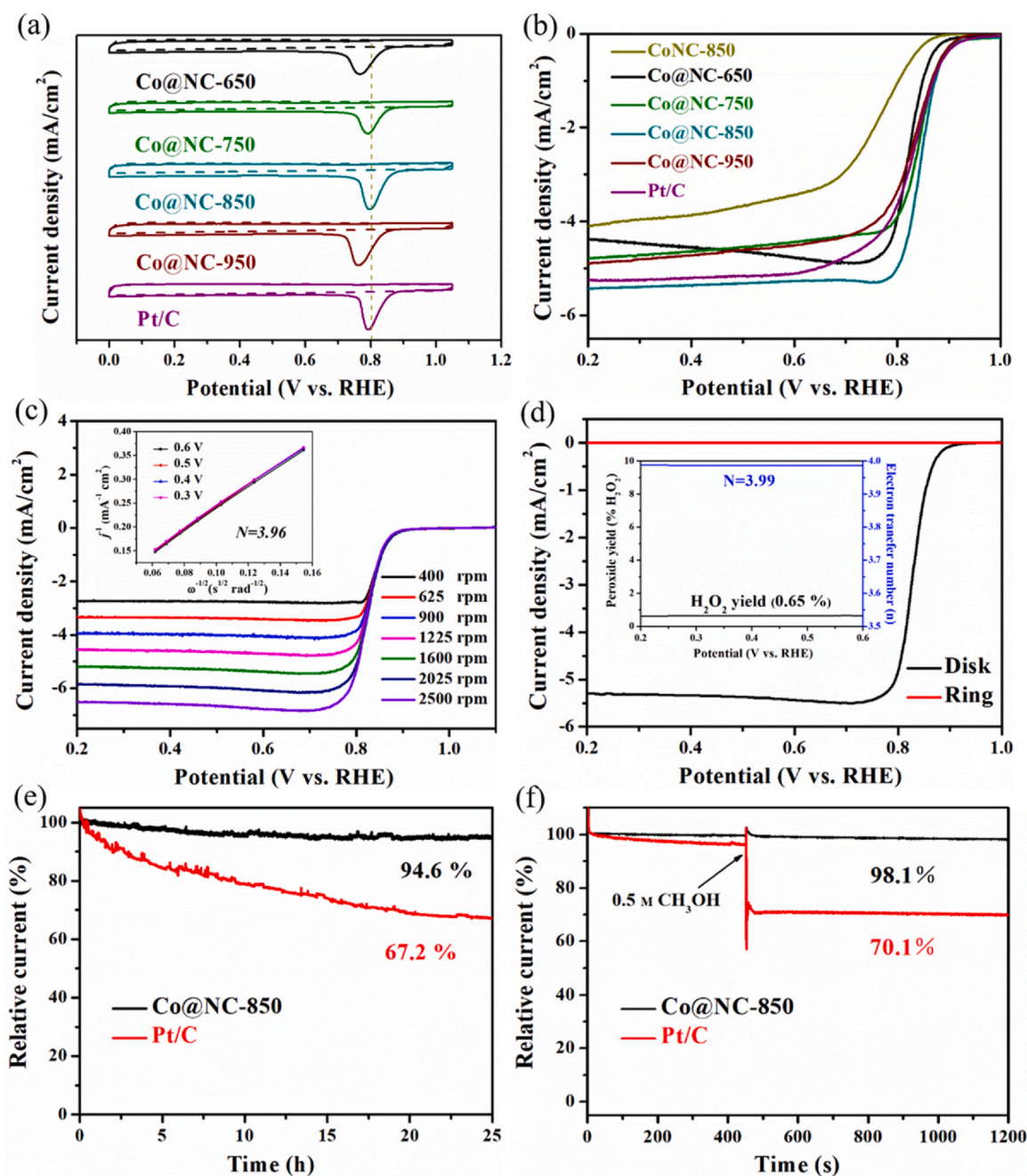
Fig. 5. (a) CV curves of Co@NC-T (T = 650, 750, 850 and 950) and Pt/C catalysts in N_2-saturated (dotted lines) and O_2-saturated (solid lines) 0.1 M KOH. (b) LSV curves of CoNC-850, Co@NC-T (T = 650, 750, 850 and 950) and Pt/C in O_2-saturated 0.1 M KOH with electrode rotating rate of 1600 rpm. (c) LSV curves at various electrode rotating rates (inset shows the corresponding Koutecky-Levich (K-L) plots at different electrode potentials, N = 3.96). (d) RRDE measurements of Co@NC-850 (inset shows the corresponding H_2O_2 yield and electron transfer number N). (e) Long-term ORR operation stability of Co@NC-850% and 20% Pt/C at 0.6 V (vs. RHE) in O_2-saturated 0.1 M KOH solution. (f) Current-time (i-t) curves for Co@NC-850% and 20% Pt/C without and with 0.5 M methanol.

apparent shift of 15 mV is observed for Pt/C (Fig. S15b). Furthermore, the structural stability of Co@NC-850 after ORR stability test was also investigated through SEM and TEM measurements. As shown in Fig. S16, the morphology of Co@NC-850 is maintained after the stability test, and the Co nanoparticles are still firmly anchored on the carbon matrix. It is well known that as for practical ORR application, the resistance ability of a catalyst to methanol cross-effect is very important. By analyzing the chronoamperometric curves with/without the addition of methanol, we carefully detected the methanol resistance of Co@NC-850. When 0.5 M methanol was injected into the KOH electrolyte, Co@NC-850 possesses an excellent methanol tolerance as confirmed by the negligible change in the

chronoamperometric curve (Fig. 5f). In contrast, the commercial Pt/C shows a sharply decayed current density in the chronoamperometric curve. Meanwhile, the CV curve of Co@NC-850 after dropping 0.5 M methanol into the electrolyte is basically consistent with the initial CV curve (Fig. S17).

3.3. OER performance of Co@NC-T

The OER activities of the Co@NC-T were also evaluated in O_2-saturated 1 M KOH solution. As depicted in Fig. 6a, the Co@NC-850 reaches a current density of 10 mA cm^{-2} at a potential ($E_{j=10}$) of 1.55 V, which is much lower than those of CoNC-850 (1.69 V), Co@
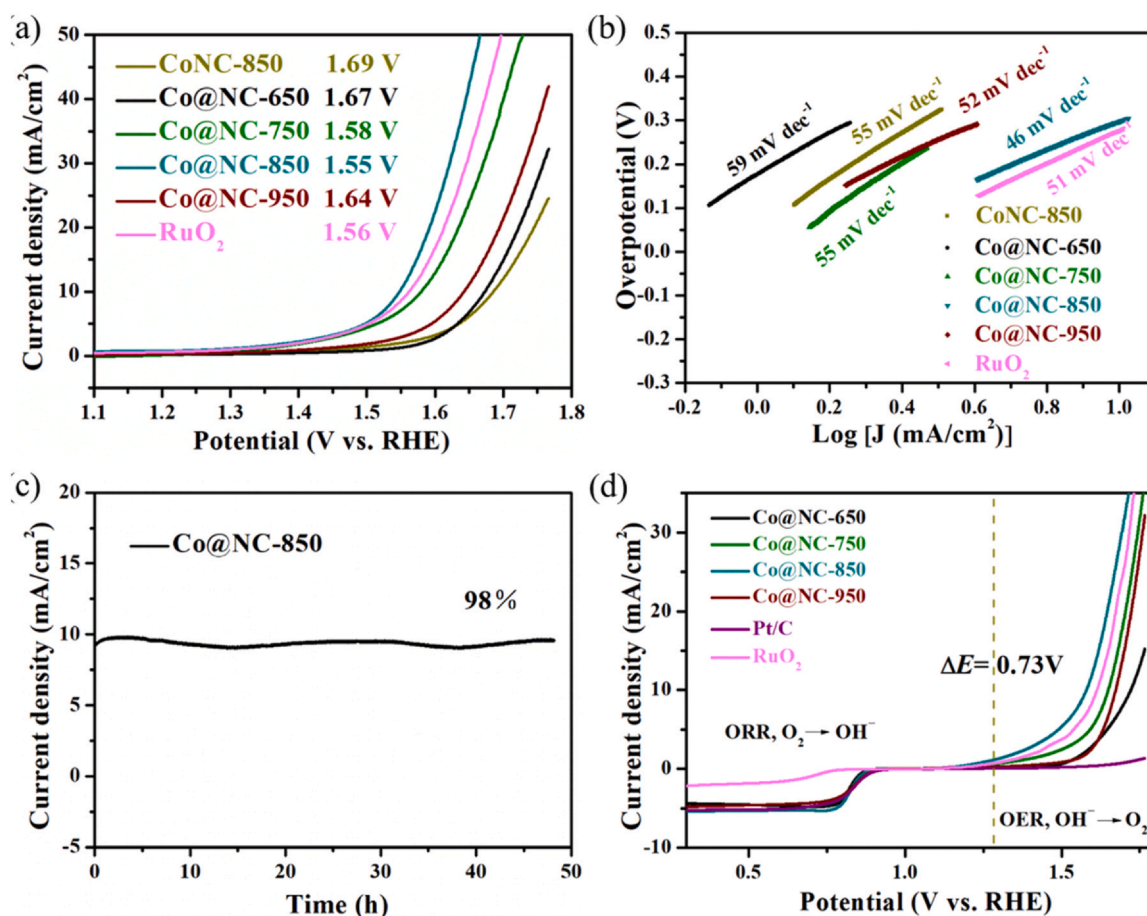
Fig. 6. (a) LSV polarization curves and (b) the corresponding Tafel plots of CoNC-850, Co@NC-T (T = 650, 750, 850 and 950) and RuO$_2$. (c) Long-term OER operation stability of Co@NC-850 at 1.55 V. (d) Overall polarization curves for ORR and OER of various catalysts at 1600 rpm (scan rate 5 mV s^{-1}).

NC-650 (1.67 V), Co@NC-750 (1.58 V), Co@NC-950 (1.64 V) and even the benchmark RuO$_2$ (1.56 V). Meanwhile, the Co@NC-850 also shows the smallest Tafel slope (46 mV dec^{-1}) as compared to those of CoNC-850 (55 mV dec^{-1}), Co@NC-650 (59 mV dec^{-1}), Co@NC-750 (55 mV dec^{-1}), Co@NC-950 (52 mV dec^{-1}) and RuO$_2$ (51 mV dec^{-1}) (Fig. 6b), suggesting the favorable OER kinetics of the Co@NC-850. The OER measurement on a glass carbon electrode (GCE) was also conducted and shown in Fig. S18. The overpotential of Co@NC-850 at the current density of 10 mA cm^{-2} on the GCE in 1 M KOH is 1.56 V, and the corresponding Tafel slope is 48 mV dec^{-1}. The slightly inferior performance on GCE with respect to that on carbon paper is probably due to the limited loading amount of catalysts and mass transport on GCE. The TOF values of Co@NC-650, 750, 850 and 950 for OER are determined to be ≈0.0004, 0.0036, 0.0084 and 0.0070 s^{-1} at 1.55 V (vs. RHE), respectively (Fig. S19). Based on the turnover frequencies calculation, the Co@NC-850 is confirmed to possess superior bifunctional activity towards oxygen electrocatalysis. As shown in Fig. S20a and Table S7, compared with all the investigated samples (including commercial RuO$_2$), the Co@NC-850 shows the lowest charge-transfer resistance (R_{ct}, 2.41 Ω). The low peak phase angle (Fig. S20b) and drastic drop in the impedance magnitude (Fig. S20c) of the Co@NC-850 further indicate that the Co@NC-850 presents the fastest charge transfer and requires the lowest activation energy for the OER. The OER stability of Co@NC-850 was evaluated by current-time (i–t) chronoamperometric method in 1 M KOH aqueous solution at 1.55 V. Fig. 6c displays that the current density of Co@NC-850 can still maintain 98% after continuous operation for 48 h. These results clearly demonstrate that the Co@NC-850 possesses outstanding OER activity and stability. The XRD and XPS of

Co@NC-850 after the chronoamperometric test were examined to confirm the stability. Fig. S21a shows the XRD pattern of the Co@NC-850 corresponding to metallic Co (JCPDS No. 15-0806) after the chronoamperometric test of OER, which indicates that N-doped carbon shell can protect the presence of the embedded cobalt nanoparticles. After the chronoamperometric test of OER, XPS analysis was conducted to check the Co valence state in Co@NC-850. As shown in Fig. S21b, the relative content of Co^0 decreases, while the contents of Co^{2+} and Co^{3+} in the Co 2p$_{3/2}$ region increase. Notably, the ratio of Co^{3+} is more than that of Co^{2+}, revealing that partial Co is oxidized to high-valence Co species at a higher potential during the OER process, probably Co (hydroxyl)oxides according to previous reports [25,71]. The oxidized high-valence Co species have been demonstrated to play an important role in promoting the OER performance.

Typically, the bifunctional activity of an oxygen electrocatalyst is evaluated by the potential gap (ΔE) between OER and ORR metrics ($\Delta E = E_{j=10}$-$E_{1/2}$). Normally, the higher activity of bifunctional electrocatalyst is consistent with the smaller potential gap. Fig. 6d shows the overall polarization curves of the Co@NC-T, Pt/C and RuO$_2$ for both OER and ORR in the potential window from 0.3 to 1.8 V in O$_2$-saturated 0.1 M KOH. For Co@NC-850, the ΔE is determined to be 0.73 V, obviously smaller than those of other Co@NC-T (0.90, 0.82, and 0.85 V for Co@NC-650, 750 and 950). Besides, the potential gap of Co@NC-850 is also smaller compared with the ΔE (~0.92 and > 0.98 V) of commercial RuO$_2$ and Pt/C, and most bifunctional non-precious-metal based carbonaceous oxygen electrocatalysts developed so far (Table S5). The comparison of the potential gap verifies the superior bifunctional activity of Co@NC-850.

4. Conclusions

In summary, we have developed an effective bifunctional oxygen electrocatalyst by constructing Co nanoparticles embedded nitrogen-doped porous carbon materials via a sol-gel route combined with pyrolysis method. Benefiting from the high content of active sites (graphitic N, pyridinic N and Co-N$_x$), large specific surface area and carbon-coating layer, the Co@NC-850 exhibits excellent activity and stability toward both ORR and OER. In 0.1 M KOH, the Co@NC-850 shows comparable ORR activity ($E_{1/2} = 0.85$ V vs. RHE) to that of commercial Pt/C and better OER activity (with an overpotential of 350 mV at 10 mA cm^{-2}) with respect to RuO$_2$. Besides, the Co@NC-850 delivers a small metric ΔE of only 0.73 V in the evaluation of the ORR-OER bifunctionality. The proposed synthetic strategy and superior ORR and OER activity promise the potential application in the oxygen reaction related energy systems.

Declaration of Competing Interest

The authors declare that they have no known competing financial interests or personal relationships that could have appeared to influence the work reported in this paper.

Acknowledgements

Appendix A. Supporting information

Supplementary data associated with this article can be found in the online version at doi:10.1016/j.jallcom.2021.160036.

References

[1] S. Dou, X. Li, L. Tao, J. Huo, S. Wang, Cobalt nanoparticle-embedded carbon nanotube/porous carbon hybrid derived from MOF-encapsulated Co$_3$O$_4$ for oxygen electrocatalysis, Chem. Commun. 52 (2016) 9727–9730.

[2] X. Zhong, W. Yi, Y. Qu, L. Zhang, H. Bai, Y. Zhu, J. Wan, S. Chen, M. Yang, L. Huang, M. Gu, H. Pan, B. Xu, Co single-atom anchored on Co$_3$O$_4$ and nitrogen-doped active carbon toward bifunctional catalyst for zinc-air batteries, Appl. Catal. B Environ. 260 (2020) 118188.

[3] X. Zhao, M. Yin, L. Ma, L. Liang, C. Liu, J. Liao, T. Lu, W. Xing, Recent advances in catalysts for direct methanol fuel cells, Energy Environ. Sci. 4 (2011) 2736–2753.

[4] J. Wu, D. Wang, S. Wan, H. Liu, C. Wang, X. Wang, An efficient cobalt phosphide electrocatalyst derived from cobalt phosphonate complex for all-pH hydrogen evolution reaction and overall water splitting in alkaline solution, Small 16 (2020) 1900550.

[5] W. Yaseen, N. Ullah, M. Xie, W. Wei, Y. Xu, M. Zahid, C.J. Oluigbo, B.A. Yusuf, J. Xie, Cobalt–Iron nanoparticles encapsulated in mesoporous carbon nanosheets: a one-pot synthesis of highly stable electrocatalysts for overall water splitting, Int. J. Hydrog. Energy 46 (2021) 5234–5249.

[6] F. Meng, H. Zhong, D. Bao, J. Yan, X. Zhang, In situ coupling of strung Co$_4$N and Intertwined N-C fibers toward free-standing bifunctional cathode for robust, efficient, and flexible Zn-air batteries, J. Am. Chem. Soc. 138 (2016) 10226–10231.

[7] K. He, J. Zai, X. Liu, Y. Zhu, A. Iqbal, T. Tadesse Tsega, Y. Zhang, N. Ali, X. Qian, One-step construction of multi-doped nanoporous carbon-based nanoarchitecture as an advanced bifunctional oxygen electrode for Zn-air batteries, Appl. Catal. B Environ. 265 (2020) 118594–118603.

[8] X. Shu, S. Chen, S. Chen, W. Pan, J. Zhang, Cobalt nitride embedded holey N-doped graphene as advanced bifunctional electrocatalysts for Zn-air batteries and overall water splitting, Carbon 157 (2020) 234–243.

[9] J. Wu, L. Hu, N. Wang, Y. Li, D. Zhao, L. Li, X. Peng, Z. Cui, L.-J. Ma, Y. Tian, X. Wang, Surface confinement assisted synthesis of nitrogen-rich hollow carbon cages with Co nanoparticles as breathable electrodes for Zn-air batteries, Appl. Catal. B Environ. 254 (2019) 55–65.

[10] Z. Jiang, W. Sun, H. Shang, W. Chen, T. Sun, H. Li, J. Dong, J. Zhou, Z. Li, Y. Wang, R. Cao, R. Sarangi, Z. Yang, D. Wang, J. Zhang, Y. Li, Atomic interface effect of a single atom copper catalyst for enhanced oxygen reduction reactions, Energy Environ. Sci. 12 (2019) 3508–3514.

[11] C. Chen, Y. Kang, Z. Huo, Z. Zhu, W. Huang, H.L. Xin, J.D. Snyder, D. Li, J.A. Herron, M. Mavrikakis, M. Chi, K.L. More, Y. Li, N.M. Markovic, G.A. Somorjai, P. Yang, V.R. Stamenkovic, Highly crystalline multimetallic nanoframes with three-dimensional electrocatalytic surfaces, Science 343 (2014) 1339–1343.

[12] H.A. Gasteiger, S.S. Kocha, B. Sompalli, F.T. Wagner, Activity benchmarks and requirements for Pt, Pt-alloy, and non-Pt oxygen reduction catalysts for PEMFCs, Appl. Catal. B Environ. 56 (2005) 9–35.

[13] Z.-X. Lu, Y. Shi, C.-F. Yan, C.-Q. Guo, Z.-D. Wang, Investigation on IrO$_2$ supported on hydrogenated TiO$_2$ nanotube array as OER electro-catalyst for water electrolysis, Int. J. Hydrog. Energy 42 (2017) 3572–3578.

[14] K.A. Stoerzinger, O. Diaz-Morales, M. Kolb, R.R. Rao, R. Frydendal, L. Qiao, X.R. Wang, N.B. Halck, J. Rossmeisl, H.A. Hansen, T. Vegge, I.E.L. Stephens, M.T.M. Koper, Y. Shao-Horn, Orientation-dependent oxygen evolution on RuO$_2$ without lattice exchange, ACS Energy Lett. 2 (2017) 876–881.

[15] W. Xia, A. Mahmood, Z. Liang, R. Zou, S. Guo, Earth-abundant nanomaterials for oxygen reduction, Angew. Chem. Int. Ed. 55 (2016) 2650–2676.

[16] Y. Lei, R. Huang, H. Xie, D. Zhang, X. Liu, Y. Si, N. Li, Electronic structure tuning of FeCo nanoparticles embedded in multi-dimensional carbon matrix for enhanced bifunctional oxygen electrocatalysis, J. Alloy. Compd. 853 (2021) 157070–157078.

[17] Zhen-Feng Huang, Jiong Wang, Yuecheng Peng, Chi-Young Jung, Adrian Fisher, Xin Wang, Design of effcient bifunctional oxygen reduction/evolution electrocatalyst: recent advances and perspectives, Adv. Energy Mater. 7 (2017) 170054.

[18] Y.B. Adegbemiga, N. Ullah, M. Xie, S. Hussain, C.J. Oluigbo, W. Yaseen, A.J. Kumar, Y. Xu, J. Xie, Ni$_3$Fe nanoparticles enclosed by B-doped carbon for efficient bifunctional performances of oxygen and hydrogen evolution reactions, J. Alloy. Compd. 835 (2020) 155267.

[19] H. Huang, X. Wei, S. Gao, Nitrogen-doped porous carbon derived from malachium aquaticum biomass as a highly efficient electrocatalyst for oxygen reduction reaction, Electrochim. Acta 220 (2016) 427–435.

[20] H.-J. Niu, A.-J. Wang, L. Zhang, J.-J. Guo, J.-J. Feng, Ultrafine NiCoP-decorated N,S,P-codoped hierarchical porous carbon nanosheets as an efficient bifunctional electrocatalyst for oxygen reduction and oxygen evolution, Mater. Chem. Front. 3 (2019) 1849–1858.

[21] K. He, T. Tadesse Tsega, X. Liu, J. Zai, X.H. Li, X. Liu, W. Li, N. Ali, X. Qian, Utilizing the space-charge region of the FeNi-LDH/CoP p-n junction to promote performance in oxygen evolution electrocatalysis, Angew. Chem. Int. Ed. 58 (2019) 11903–11909.

[22] X. Wang, J. Xu, M. Zhi, Z. Hong, F. Huang, Synthesis of Co$_2$P nanoparticles decorated nitrogen, phosphorus Co-doped Carbon-CeO$_2$ composites for highly efficient oxygen reduction, J. Alloy. Compd. 801 (2019) 192–198.

[23] C.J. Oluigbo, N. Ullah, M. Xie, C.C. Okoye, B.A. Yusuf, W. Yaseen, J.K. Alagarasan, K. Rajalakshmi, Y. Xu, J. Xie, Incorporation of pyridinic and graphitic N to Ni@CNTs: as a competent electrocatalyst for hydrogen evolution reaction, Int. J. Energy Res. 44 (2020) 9157–9165.

[24] I.S. Amiinu, X. Liu, Z. Pu, W. Li, Q. Li, J. Zhang, H. Tang, H. Zhang, S. Mu, From 3D ZIF nanocrystals to Co-N$_x$/C nanorod array electrocatalysts for ORR, OER, and Zn-air batteries, Adv. Funct. Mater. 28 (2018) 1704638.

[25] H.-J. Niu, A.-J. Wang, L. Zhang, J.-J. Feng, Bioinspired one-step pyrolysis fabrication of 3D porous Co, N, P-doped carbon nanosheets with enriched CoN$_x$ active sites as high-performance bifunctional oxygen electrocatalyst for rechargeable Zn–air battery, ACS Appl. Energy Mater. 3 (2020) 2781–2790.

[26] X. Qiao, S. Liao, R. Zheng, Y. Deng, H. Song, L. Du, Cobalt and nitrogen codoped graphene with inserted carbon nanospheres as an efficient bifunctional electrocatalyst for oxygen reduction and evolution, ACS Sustain. Chem. Eng. 4 (2016) 4131–4136.

[27] D. He, Y. Xiong, J. Yang, X. Chen, Z. Deng, M. Pan, Y. Li, S. Mu, Nanocarbon-intercalated and Fe–N-codoped graphene as a highly active noble-metal-free bifunctional electrocatalyst for oxygen reduction and evolution, J. Mater. Chem. A 5 (2017) 1930–1934.

[28] Y. Nie, L. Li, Z. Wei, Recent advancements in Pt and Pt-free catalysts for oxygen reduction reaction, Chem. Soc. Rev. 44 (2015) 2168–2201.

[29] K.J. Lee, D.Y. Shin, A. Byeon, A. Lim, Y.S. Jo, A. Begley, D.H. Lim, Y.E. Sung, H.S. Park, K.H. Chae, S.W. Nam, K.Y. Lee, J.Y. Kim, Hierarchical cobalt-nitride and -oxide co-doped porous carbon nanostructures for highly efficient and durable bifunctional oxygen reaction electrocatalysts, Nanoscale 9 (2017) 15846–15855.

[30] S. Li, W. Chen, H. Pan, Y. Cao, Z. Jiang, X. Tian, X. Hao, T. Maiyalagan, Z.-J. Jiang, FeCo alloy nanoparticles coated by an ultrathin N-doped carbon layer and encapsulated in carbon nanotubes as a highly efficient bifunctional air electrode for rechargeable Zn-air batteries, ACS Sustain. Chem. Eng. 7 (2019) 8530–8541.

[31] X. Zhong, Y. Jiang, X. Chen, L. Wang, G. Zhuang, X. Li, J.-g Wang, Integrating cobalt phosphide and cobalt nitride-embedded nitrogen-rich nanocarbons: high-performance bifunctional electrocatalysts for oxygen reduction and evolution, J. Mater. Chem. A 4 (2016) 10575–10584.

[32] X.R. Wang, J.Y. Liu, Z.W. Liu, W.C. Wang, J. Luo, X.P. Han, X.W. Du, S.Z. Qiao, J. Yang, Identifying the key role of pyridinic-N-Co bonding in synergistic electrocatalysis for reversible ORR/OER, Adv. Mater. 30 (2018) 1800005.

[33] Y. Zheng, Y. Jiao, Y. Zhu, Q. Cai, A. Vasileff, L.H. Li, Y. Han, Y. Chen, S.Z. Qiao, Molecule-Level g-C$_3$N$_4$ coordinated transition metals as a new class of electrocatalysts for oxygen electrode reactions, J. Am. Chem. Soc. 139 (2017) 3336–3339.

[34] W.J. Jiang, L. Gu, L. Li, Y. Zhang, X. Zhang, L.J. Zhang, J.Q. Wang, J.S. Hu, Z. Wei, L.J. Wan, Understanding the high activity of Fe-N-C electrocatalysts in oxygen reduction: Fe/Fe$_3$C nanoparticles boost the activity of Fe-N$_x$, J. Am. Chem. Soc. 138 (2016) 3570–3578.

[35] P. Yin, T. Yao, Y. Wu, L. Zheng, Y. Lin, W. Liu, H. Ju, J. Zhu, X. Hong, Z. Deng, G. Zhou, S. Wei, Y. Li, Single cobalt atoms with precise N-coordination as superior

oxygen reduction reaction catalysts, Angew. Chem. Int. Ed. 55 (2016) 10800–10805.

[36] S. Wan, J. Wu, D. Wang, H. Liu, Z. Zhang, J. Ma, C. Wang Co/N-doped carbon nanotube arrays grown on 2D MOFs-derived matrix for boosting the oxygen reduction reaction in alkaline and acidic media, Chin. Chem. Lett. https://doi.org/10.1016/j.cclet.2020.04.040.

[37] B.Y. Xia, Y. Yan, N. Li, H.B. Wu, X.W. Lou, X. Wang, A metal–organic framework-derived bifunctional oxygen electrocatalyst, Nat. Energy 1 (2016) 15006.

[38] Y. Chen, R. Gao, S. Ji, H. Li, K. Tang, P. Jiang, H. Hu, Z. Zhang, H. Hao, Q. Qu, X. Liang, W. Chen, J. Dong, D. Wang, Y. Li, Atomic-level modulation of electronic density at cobalt single-atom sites derived from metal-organic frameworks: enhanced oxygen reduction performance, Angew. Chem. Int. Ed. 59 (2020) 2–12.

[39] N. Mahmood, Y. Yao, J.W. Zhang, L. Pan, X. Zhang, J.J. Zou, Electrocatalysts for hydrogen evolution in alkaline electrolytes: mechanisms, challenges, and prospective solutions, Adv. Sci. 5 (2018) 1700464.

[40] W. Wang, W. Chen, P. Miao, J. Luo, Z. Wei, S. Chen, NaCl crystallites as dual-functional and water-removable templates to synthesize a three-dimensional graphene-like macroporous Fe-N-C catalyst, ACS Catal. 7 (2017) 6144–6149.

[41] Q. Shao, Y. Li, X. Cui, T. Li, H.-g Wang, Y. Li, Q. Duan, Z. Si, Metallophthalocyanine-based polymer-derived Co_2P nanoparticles anchoring on doped graphene as high-efficient trifunctional electrocatalyst for Zn-air batteries and water splitting, ACS Sustain. Chem. Eng. 8 (2020) 6422–6432.

[42] H. Zhao, C.-C. Weng, J.-T. Ren, L. Ge, Y.-P. Liu, Z.-Y. Yuan, Phosphonate-derived nitrogen-doped cobalt phosphate/carbon nanotube hybrids as highly active oxygen reduction reaction electrocatalysts, Chin. J. Catal. 41 (2020) 259–267.

[43] B. Chen, X. He, F. Yin, H. Wang, D.-J. Liu, R. Shi, J. Chen, H. Yin, MO-Co@N-doped carbon (M = Zn or Co): vital roles of inactive Zn and highly efficient activity toward oxygen reduction/evolution reactions for rechargeable Zn-Air battery, Adv. Funct. Mater. 27 (2017) 1700795.

[44] Q. Zhou, Z. Zhang, J. Cai, B. Liu, Y. Zhang, X. Gong, X. Sui, A. Yu, L. Zhao, Z. Wang, Z. Chen, Template-guided synthesis of Co nanoparticles embedded in hollow nitrogen doped carbon tubes as a highly efficient catalyst for rechargeable Zn-air batteries, Nano Energy 71 (2020) 104592.

[45] C. Belkessam, S. Bencherif, M. Mechouet, N. Idiri, J. Ghilane, The effect of heteroatom doping on nickel cobalt oxide electrocatalysts for oxygen evolution and reduction reactions, ChemPlusChem 85 (2020) 1710–1718.

[46] J.X. Flores-Lasluisa, F. Huerta, D. Cazorla-Amoros, E. Morallon, Carbon material and cobalt-substitution effects in the electrochemical behavior of $LaMnO_3$ for ORR and OER, Nanomaterials 10 (2020) 2394.

[47] L. Yu, N. Xu, T. Zhu, Z. Xu, M. Sun, D. Geng, $La_{0.4}Sr_{0.6}Co_{0.7}Fe_{0.2}Nb_{0.1}O_{3-\delta}$ perovskite prepared by the sol-gel method with superior performance as a bifunctional oxygen electrocatalyst, Int. J. Hydrog. Energy 45 (2020) 30583–30591.

[48] Y. Guo, P. Yuan, J. Zhang, Y. Hu, I.S. Amiinu, X. Wang, J. Zhou, H. Xia, Z. Song, Q. Xu, S. Mu, Carbon nanosheets containing discrete $Co-N_x-B_y-C$ active sites for efficient oxygen electrocatalysis and rechargeable Zn-air batteries, ACS Nano 12 (2018) 1894–1901.

[49] S. Ma, G.A. Goenaga, A.V. Call, D.J. Liu, Cobalt imidazolate framework as precursor for oxygen reduction reaction electrocatalysts, Chem. Eur. J. 17 (2011) 2063–2067.

[50] X. Wang, J. Zhou, H. Fu, W. Li, X. Fan, G. Xin, J. Zheng, X. Li, MOF derived catalysts for electrochemical oxygen reduction, J. Mater. Chem. A 2 (2014) 14064–14070.

[51] Y. Hao, Z. Lu, G. Zhang, Z. Chang, L. Luo, X. Sun, Cobalt-embedded nitrogen-doped carbon nanotubes as high-performance bifunctional oxygen catalysts, Energy Technol. 5 (2017) 1265–1271.

[52] H. Jiang, Y. Liu, W. Li, J. Li, Co nanoparticles confined in 3D nitrogen-doped porous carbon foams as bifunctional electrocatalysts for long-life rechargeable Zn-air batteries, Small 14 (2018) 1703739.

[53] H.-S. Lu, H. Zhang, R. Liu, X. Zhang, H. Zhao, G. Wang, Macroscale cobalt-MOFs derived metallic Co nanoparticles embedded in N-doped porous carbon layers as efficient oxygen electrocatalysts, Appl. Surf. Sci. 392 (2017) 402–409.

[54] L. Zhang, X. Wang, R. Wang, M. Hong, Structural evolution from metal−organic framework to hybrids of nitrogen-doped porous carbon and carbon nanotubes for enhanced oxygen reduction activity, Chem. Mater. 27 (2015) 7610–7618.

[55] Z. Hu, Z. Zhang, Z. Li, M. Dou, F. Wang, One-step conversion from core-shell metal-organic framework materials to cobalt and nitrogen codoped carbon nanopolyhedra with hierarchically porous structure for highly efficient oxygen reduction, ACS Appl. Mater. Interfaces 9 (2017) 16109–16116.

[56] W. Wan, X. Liu, H. Li, X. Peng, D. Xi, J. Luo, 3D carbon framework-supported CoNi nanoparticles as bifunctional oxygen electrocatalyst for rechargeable Zn-air batteries, Appl. Catal. B Environ. 240 (2019) 193–200.

[57] J. Chen, X. Yuan, F. Lyu, Q. Zhong, H. Hu, Q. Pan, Q. Zhang, Integrating MXene nanosheets with cobalt-tipped carbon nanotubes for an efficient oxygen reduction reaction, J. Mater. Chem. A 7 (2019) 1281–1286.

[58] C. Xiao, J. Luo, M. Tan, Y. Xiao, B. Gao, Y. Zheng, B. Lin, Co/CoN decorated nitrogen-doped porous carbon derived from melamine sponge as highly active oxygen electrocatalysts for zinc-air batteries, J. Power Sources 453 (2020) 227900.

[59] C. Guan, A. Sumboja, W. Zang, Y. Qian, H. Zhang, X. Liu, Z. Liu, D. Zhao, S.J. Pennycook, J. Wang, Decorating Co/CoN_x nanoparticles in nitrogen-doped carbon nanoarrays for flexible and rechargeable zinc-air batteries, Energy Storage Mater. 16 (2019) 243–250.

[60] Z. Liang, Z. Zhang, C. Yuan, W. Zhang, H. Zheng, R. Cao, PVP-assisted transformation of a metal-organic framework into Co-embedded N-enriched meso/microporous carbon materials as bifunctional electrocatalysts, Chem. Commun. 54 (2018) 7519–7522.

[61] C.-Y. Su, H. Cheng, W. Li, Z.-Q. Liu, N. Li, Z. Hou, F.-Q. Bai, H.-X. Zhang, T.-Y. Ma, Fluorescent nanodiamonds enable quantitative tracking of human mesenchymal stem cells in miniature pigs, Sci. Rep. 7 (2017) 45607.

[62] Y. Li, B. Jia, Y. Fan, K. Zhu, G. Li, C.-Y. Su, Bimetallic zeolitic imidazolite framework derived carbon nanotubes embedded with Co nanoparticles for efficient bifunctional oxygen electrocatalyst, Adv. Energy Mater. 8 (2018) 1702048.

[63] X. Song, L. Guo, X. Liao, J. Liu, J. Sun, X. Li, Hollow carbon nanopolyhedra for enhanced electrocatalysis via confined hierarchical porosity, Small 13 (2017) 1700238.

[64] L.-F. Zhai, S.-Y. Kong, H. Zhang, W. Tian, M. Sun, H. Sun, S. Wang, Facile synthesis of Co-N-rGO composites as an excellent electrocatalyst for oxygen reduction reaction, Chem. Eng. Sci. 194 (2019) 45–53.

[65] J.F. Callejas, C.G. Read, C.W. Roske, N.S. Lewis, R.E. Schaak, Synthesis, characterization, and properties of metal phosphide catalysts for the hydrogen-evolution reaction, Chem. Mater. 28 (2016) 6017–6044.

[66] G. Zhang, G. Wang, Y. Liu, H. Liu, J. Qu, J. Li, Highly active and stable catalysts of phytic Acid-Derivative transition metal phosphides for full water splitting, J. Am. Chem. Soc. 138 (2016) 14686–14693.

[67] H. Jiang, C. Li, H. Shen, Y. Liu, W. Li, J. Li, Supramolecular gel-assisted synthesis Co_2P particles anchored in multielement co-doped graphene as efficient bifunctional electrocatalysts for oxygen reduction and evolution, Electrochim. Acta 231 (2017) 344–353.

[68] W. Zang, A. Sumboja, Y. Ma, H. Zhang, Y. Wu, S. Wu, H. Wu, Z. Liu, C. Guan, J. Wang, S.J. Pennycook, Single Co atoms anchored in porous N-Doped carbon for efficient zinc−air battery cathodes, ACS Catal. 8 (2018) 8961–8969.

[69] Y. Guo, P. Yuan, J. Zhang, H. Xia, F. Cheng, M. Zhou, J. Li, Y. Qiao, S. Mu, Q. Xu, Co_2P-CoN double active centers confined in N-doped carbon nanotube: heterostructural engineering for trifunctional catalysis toward HER, ORR, OER, and Zn-air batteries driven water splitting, Adv. Funct. Mater. 28 (2018) 1805641.

[70] X. Wu, S. Chen, Y. Feng, Q. Yuan, J. Gao, Y. Chen, Y. Huang, Y.B. He, W. Gan, Microwave-assisted synthesis of carbon nanotubes threaded core-shell CoP/Co-N-C@CNT and its performance as an efficient bifunctional oxygen catalyst for the rechargeable zinc-air battery, Mater. Today Phys. 9 (2019) 100132.

[71] H. Guo, Q. Feng, J. Zhu, J. Xu, Q. Li, S. Liu, K. Xu, C. Zhang, T. Liu, Cobalt nanoparticle-embedded nitrogen-doped carbon/carbon nanotube frameworks derived from a metal−organic framework for tri-functional ORR, OER and HER electrocatalysis, J. Mater. Chem. A 7 (2019) 3664–3672.